Landau theory of topological defects in multiferroic hexagonal manganites

Artyukhin, Sergey; Delaney, Kris T.; Spaldin, Nicola A.; Mostovoy, Maxim

Published in:
Nature Materials

DOI:
10.1038/nmat3786

Publication date:
2014

ARTICLES
PUBLISHED ONLINE: 27 OCTOBER 2013 | DOI: 10.1038/NMAT3786
nature materials

Landau theory of topological defects in multiferroic hexagonal manganites

Sergey Artyukhin[1,2], Kris T. Delaney[3], Nicola A. Spaldin[4] and Maxim Mostovoy[1]*

Topological defects in ordered states with spontaneously broken symmetry often have unusual physical properties, such as fractional electric charge or a quantized magnetic field flux, originating from their non-trivial topology. Coupled topological defects in systems with several coexisting orders give rise to unconventional functionalities, such as the electric-field control of magnetization in multiferroics resulting from the coupling between the ferroelectric and ferromagnetic domain walls. Hexagonal manganites provide an extra degree of freedom: in these materials, both ferroelectricity and magnetism are coupled to an additional, non-ferroelectric structural order parameter. Here we present a theoretical study of topological defects in hexagonal manganites based on Landau theory with parameters determined from first-principles calculations. We explain the observed flip of electric polarization at the boundaries of structural domains, the origin of the observed discrete vortices, and the clamping between ferroelectric and antiferromagnetic domain walls. We show that structural vortices induce magnetic ones and that, consistent with a recent experimental report, ferroelectric domain walls can carry a magnetic moment.

Recent experimental and theoretical advances in the field of multiferroics have clarified the microscopic mechanisms of coupling between ferroelectricity and magnetism in bulk materials and led to the discovery of many families of materials in which ferroelectricity is induced by a spin ordering. Examples include the orthorhombic rare-earth manganites, spinels, hexaferrites and delafossites, which usually have spin orderings of the cycloidal or conical spiral type[1–3]. The resulting electric polarization is highly susceptible to an applied magnetic field and can be easily rotated or reversed[4–6]. However, this magnetically induced polarization is usually too small to allow manipulation of spin states by an applied voltage. Much larger electric polarizations are found in multiferroics such as $BiFeO_3$ and the hexagonal rare-earth manganites, in which ferroelectricity results not from spin ordering but from electronic and lattice instabilities[7–9]. Yet in these materials, the electric control of magnetism is not straightforward[10–12], because the direction of spins in the magnetically ordered state is not correlated with the sign of the macroscopic electric polarization (materials where such a correlation does exist are discussed for example in ref. 13).

Although enhancing bulk couplings between polarization and magnetism is difficult, practical switching of a ferroic order parameter with an applied field invariably involves motion of the domain walls. Magnetoelectric switching therefore depends crucially on interactions between ferroelectric and ferromagnetic domain walls, which are not as well understood. In this context, the observed clamping between ferroelectric and antiferromagnetic domain walls in multiferroic hexagonal manganites[14] provides a unique prototype for investigation.

The hexagonal manganites, $RMnO_3$, where R denotes a small-radius rare earth ion (Dy, Ho, Er, Tm, Yb, Lu), Y or Sc, are improper ferroelectrics; electric polarization appears as a by-product of a primary structural transition[7]. The crystal structure consists of corner-sharing MnO_5 trigonal bipyramids, which form triangular layers, separated by layers of R ions. The structural transition above 1,000 K results in periodic tilts of the MnO_5 bipyramids and displacements of the R ions along the c axis normal to the layers[15,16]. This periodic $\sqrt{3} \times \sqrt{3}$ lattice distortion makes the size of the unit cell three times larger and is often referred to as the trimerization transition (Fig. 1a–c). The anharmonic coupling between the trimerization mode and a polar optical phonon mode induces the observed electric polarization along the c axis, $P_c \sim 5.5\,\mu C\,cm^{-2}$ (ref. 17).

At much lower temperatures, ~100 K, an antiferromagnetic ordering of Mn spins emerges. Although there is a large body of evidence for the strong interplay between the microscopic spin, charge and lattice degrees of freedom in hexagonal manganites[16,18–20], the sign of the overall antiferromagnetic order parameter is decoupled from the direction of the macroscopic electric polarization, as such correlation is forbidden by symmetry. It therefore came as a surprise when nonlinear optical measurements of $YMnO_3$ demonstrated that ferroelectric domain walls are locked to magnetic ones[14]. Furthermore, this clamping was found to be non-reciprocal, as free magnetic domain walls, not associated with the electric polarization reversals, were also observed. Proposals for the clamping mechanism have included strain mediation[21] and modification of spin interactions at ferroelectric walls[22,23].

Recently, new observational evidence has shed light on the mechanism for clamping. A combination of conducting atomic-force microscopy and transmission-electron microscopy demonstrated that the ferroelectric domain walls are pinned to the boundaries of the structural domains that appear on transition to the trimerized state[24,25]. These measurements also revealed intricate patterns of unusual line defects. These so-called cloverleaf defects[24,25], at which six different structural and ferroelectric domains merge, have also been seen in piezoresponse force microscopy[26,27]. In ref. 28 it was suggested that the line defects are discrete analogues of vortices, and that the change of polarization sign at structural domain boundaries is a consequence of the special form of the coupling between the lattice distortion and electric

[1]Zernike Institute for Advanced Materials, University of Groningen, Nijenborgh 4, 9747 AG, Groningen, The Netherlands, [2]Department of Physics and Astronomy, Rutgers University, Piscataway, New Jersey 08854, USA, [3]Materials Research Laboratory, University of California, Santa Barbara, California 93106-5121, USA, [4]Materials Theory, ETH Zurich, Wolfgang-Pauli-Strasse 27, CH-8093 Zurich, Switzerland. *e-mail: M.Mostovoy@rug.nl

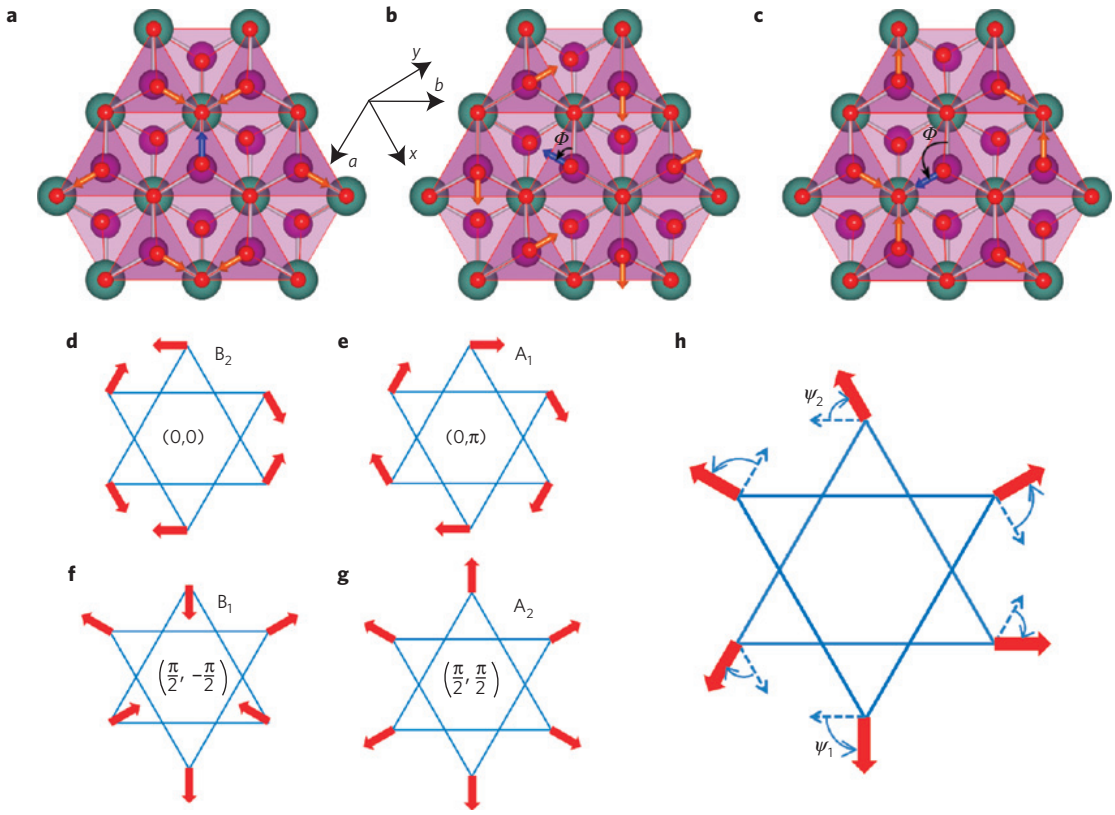

Figure 1 | Structural and magnetic angles. a–c, Projections of the displacements of apical oxygen ions on the *ab* plane in the trimerized state indicated by arrows. One ion (blue arrow) is chosen to define the trimerization phase Φ. Shown are the α_+ state with $\Phi = 0$ (**a**), the γ_- state with $\Phi = \pi/3$ (**b**) and the β_+ state with $\Phi = 2\pi/3$ (**c**). Also shown are the displacements of apical oxygen ions in an adjacent Mn–O layer (lighter triangles). Purple, red and green spheres represent Mn, oxygen and rare earth ions, respectively. **d–g**, The four magnetic states of hexagonal manganites with the spin directions indicated by red arrows and the corresponding values of the angles (χ_1, χ_2), where $\chi_{1,2} = \psi_{1,2} - \Phi$ (see text). **h**, The angles ψ_1 and ψ_2 describing the rotations of spins in magnetic domain walls ($\psi_1, \psi_2 > 0$ correspond to the clockwise (anticlockwise) rotation in even (odd) Mn layers).

Table 1 | Transformation properties under the generators of the $P6_3/mmc$ space group.

	S_a	3_c	$\tilde{2}_c$	m_{a+b}	I	T
Φ	$\Phi+2\pi/3$	Φ	$-\Phi$	$-\Phi$	$\pi-\Phi$	Φ
ψ_1	$\psi_1+2\pi/3$	ψ_1	$\pi-\psi_2$	$-\psi_1$	$-\psi_2$	$\psi_1+\pi$
ψ_2	$\psi_2+2\pi/3$	ψ_2	$\pi-\psi_1$	$-\psi_2$	$-\psi_1$	$\psi_2+\pi$
P_c	$+P_c$	$+P_c$	$+P_c$	$+P_c$	$-P_c$	$+P_c$
H_c	$+H_c$	$+H_c$	$+H_c$	$-H_c$	$+H_c$	$-H_c$

Translation $S_a = (x+1, y, z)$, three-fold axis $3_c = (-y, x-y, z)$, two-fold screw axis $\tilde{2}_c = (-x, -y, z+1/2)$, mirror plane $m_{a+b} = (-y, -x, z)$, inversion $I = (-x, -y, -z)$, and the time reversal operation T.

polarization originating from the improper nature of ferroelectricity in hexagonal manganites[7,17]. These results put the clamping between the ferroelectric and antiferromagnetic domain walls into an entirely new perspective.

In this article we study the interplay between structural, ferroelectric and magnetic defects in hexagonal manganites using an expansion of the free energy in powers of the corresponding order parameters and their gradients. Based on symmetries of ordered states of these materials, this approach allows us to identify stable topological defects and describe their mutual interactions in the most economical way. Ref. 17 discussed the Landau theory of improper ferroelectricity for spatially uniform states of hexagonal manganites. Extracting parameters of the Landau expansion from first-principles studies of $YMnO_3$, it was shown that polarization emerges owing to a nonlinear coupling to the trimerization mode. We extend this theory to inhomogeneous topological defects and include spin degrees of freedom to study effects of the structural domain walls and vortices on magnetic ordering.

Landau theory

In the trimerized state, three neighbouring MnO_5 bipyramids tilt towards (or away from) their common equatorial oxygen atom[7] (Fig. 1a–c). As a consequence of the hexagonal structure of Mn–O layers, there are six distinct trimerized states, corresponding to six degenerate minima of the lattice energy. Being a periodic lattice modulation in a layered system, the trimerization is described entirely by the amplitude Q and phase Φ. The physical meaning of the phase Φ is the azimuthal angle describing the in-plane displacements of apical oxygens (Fig. 1a–c). The minimal-energy states can then be labelled by the six values of the phase: $0, \pm\pi/3, \pm 2\pi/3$ and π. At the structural domain boundaries Φ varies spatially between two of these six values.

Microscopically, the trimerization is the condensation of the zone-boundary K_3 mode with wavevector $\mathbf{q} = (1/3, 1/3, 0)$, which breaks the $P6_3/mmc$ symmetry of the undistorted phase lowering it to $P6_3cm$. Similarly, the spontaneous electric polarization P_c is proportional to the amplitude of the zone-centre mode $\mathcal{P}$ with Γ_2^- symmetry. This polar mode is stable in the $P6_3/mmc$ structure, but is nonlinearly coupled to the unstable K_3 mode, and therefore appears together with the trimerization.

Table 2 | Parameters of the phenomenological expansion of the free energy equation (1) obtained from *ab initio* calculations.

$a = -2.626\ \text{eV Å}^{-2}$	$b = 3.375\ \text{eV Å}^{-4}$	$c = 0.117\ \text{eV Å}^{-6}$	$c' = 0.108\ \text{eV Å}^{-6}$
$a_P = 0.866\ \text{eV Å}^{-2}$	$g = 1.945\ \text{eV Å}^{-4}$	$g' = 9.931\ \text{eV Å}^{-4}$	
$s^z_Q = 15.40\ \text{eV}$	$s^x_Q = 5.14\ \text{eV}$	$s^z_P = 52.70\ \text{eV}$	$s^x_P = -8.88\ \text{eV}$

All parameters are calculated per unit cell of the trimerized lattice with the volume $V = 365.14\ \text{Å}^3$ containing 6 formula units. The spatially dependent polarization P_c is related to the local amplitude of the polar mode $\mathcal{P}$ by $P_c = V^{-1}\tilde{Z}^*\mathcal{P}$, where $\tilde{Z}^* = 9.031e$ is the effective charge of the polar mode computed from first principles calculations using a Berry-phase approach[47]. Owing to the negative stiffness, s^x_P, of the polar mode, the term $1/2t^x_P[(\partial^2/\partial x^2 + \partial^2/\partial y^2)\mathcal{P}]^2$ with $t^x_P = 73.56\ \text{eV Å}^2$ was added to equation (1) to calculate the structure of the domain wall shown in Fig. 3a.

The free-energy expansion in powers of Q, Φ, $\mathcal{P}$, and their gradients,

$$f = \frac{a}{2}Q^2 + \frac{b}{4}Q^4 + \frac{Q^6}{6}(c + c'\cos 6\Phi) - gQ^3\mathcal{P}\cos 3\Phi + \frac{g'}{2}Q^2\mathcal{P}^2 + \frac{a_\mathcal{P}}{2}\mathcal{P}^2 + \frac{1}{2}\sum_{i=x,y,z}\left[s^i_Q(\partial_i Q\partial_i Q + Q^2\partial_i\Phi\partial_i\Phi) + s^i_\mathcal{P}\partial_i\mathcal{P}\partial_i\mathcal{P}\right], \quad (1)$$

is obtained using the transformation properties of the trimerization phase Φ and the polarization P_c under the generators of the high-temperature space group summarized in Table 1. We consider only the lowest-order stiffness terms accounting for the energy cost of spatial variations of Q, Φ and $\mathcal{P}$. Here $\partial_i = (\partial/\partial x_i)$, (x,y) are the Cartesian coordinates in the ab plane (Fig. 1), and by symmetry, $s^x_Q = s^y_Q$ and $s^x_\mathcal{P} = s^y_\mathcal{P}$.

The trimerization phase Φ and the stiffness terms, s_Q and $s_\mathcal{P}$, not considered in ref. 17, play an important role in the theory of topological defects. In particular, the form of the nonlinear coupling, $-gQ^3\mathcal{P}\cos 3\Phi$, giving rise to improper ferroelectricity, implies that for $g > 0$ the electric polarization induced in the states with $\Phi = 0, +2\pi/3$ and $-2\pi/3$ is positive (the α_+, β_+ and γ_+ phases[24,28]), whereas for $+\pi/3, \pi$ and $-\pi/3$ it is negative (the γ_-, α_- and β_- phases). In other words, neighbouring trimerization phases, separated by $\Delta\Phi = \pi/3$, have opposite electric polarizations.

The numerical values of the parameters a, b and so on in equation (1) for $YMnO_3$ are listed in Table 2. To determine them, we performed *ab initio* supercell calculations for the various lattice distortions (Methods). In particular, Fig. 2a shows the variation of the total energy with respect to the magnitude of Q for two chosen values of Φ and $\mathcal{P} = 0$. It is clear that in the physically relevant range of Q, the total energy depends very weakly on Φ. The Φ-dependence of the energy $f(Q, \Phi, \mathcal{P} = 0)$ first appears in the sixth-order of the expansion in powers of Q and the corresponding coefficient c' is small. The energy landscape in the (Q, Φ) plane therefore essentially has a rotationally invariant Mexican hat shape with no energy barriers separating the six structural domains and, hence, no domain walls. The only stable topological defects in this case are vortices with the continuously varying phase Φ, similar to vortices in superfluid helium.

In reality, the Φ-rotation of the tilted bipyramids is not a zero mode, because an additional $\cos 6\Phi$ term is generated by minimizing f with respect to $\mathcal{P}$ and eliminating $\mathcal{P}$ from equation (1), which lowers the energy by $(g^2Q^6(\cos 6\Phi + 1))/4(g'Q^2 + a_\mathcal{P})$. Figure 2c shows the dependence of the total energy on $\mathcal{P}$ for $\Phi = 0$ (at which the energy has minimum) and $\Phi = \pi/6$ (at the top of the barrier separating two minimal-energy states). Clearly, the anharmonic coupling between Q and $\mathcal{P}$ results in a strong Φ dependence of the energy. Therefore, even though the emergence of ferroelectricity in hexagonal manganites is improper, the coupling of trimerization to polarization is the only factor that determines the energetic barriers between different trimerized states, and is responsible for replacing the accidental continuous XY symmetry of f with the discrete Z_6 symmetry.

Topological defects

This has a strong effect on the structure of topological defects in the trimerized state, which can be described as trajectories in the (Q, Φ)-plane minimizing the energy for given initial and final conditions. For example, a structural domain wall corresponds to a path connecting two energy minima. The shortest path connecting two neighbouring states whose trimerization angles differ by $\Delta\Phi = \pm\pi/3$ (Fig. 2d) is the lowest-energy domain wall. This path follows the bottom fold of the Mexican hat where the potential barrier between the two minima is the lowest, so that the amplitude of the trimerization Q in the wall is close to its bulk value. Figure 3a,b shows the coordinate dependence of Φ and Q across domain walls obtained by numerical free-energy minimization. The nonlinear coupling to polarization makes the structural domain walls sharp (their width is 5–10 Å) and the trimerization amplitude Q is indeed nearly constant across the wall. These conclusions agree with the results of direct first-principles calculations of the domain wall structure[29]. It is interesting to note that domains walls connecting states with equal trimerization angle and opposite polarization (for example, α_+ and α_-) are enormously disfavoured; the centre of the wall in that case would correspond to an untrimerized (and paraelectric) state. In reality, such a situation is unstable versus decay into three domain walls with spontaneous insertion of two extra domains.

As the neighbouring energy minima separated by $\Delta\Phi = \pm\pi/3$ have anti-parallel electric polarizations, the structural domain wall is at the same time a ferroelectric domain wall (Fig. 3a,b). The improper nature of ferroelectricity in hexagonal manganites forbids purely ferroelectric domain walls, that is, the reversals of P_c within one structural domain, because the sign of P_c is uniquely determined by the sign of $\cos 3\Phi$. Furthermore, the structural domain walls with $\Delta\Phi = 2\pi/3$, separating states with the same electric polarization, are unstable: they decay into lowest-energy domain walls with $\Delta\Phi = \pi/3$ that repel each other when they overlap owing to the nonlinear dependence of the free energy on Φ and $\nabla\Phi$. This explains the clamping between the structural and ferroelectric domain walls observed in ref. 24.

The structural domain walls terminate either at the surface of the sample or at another type of stable topological defect—the structural vortex or anti-vortex, shown in Fig. 3c. At the vortex line, where the trimerization amplitude Q vanishes, all six structural domains meet in such an order that the trimerization phase Φ changes by 2π around a contour encircling the vortex line[28]. Such a defect cannot be unwound and can be annihilated only by an anti-vortex, around which the phase changes by -2π (Fig. 3c). Away from the core, the trimerization phase Φ varies strongly only at the six radial domain walls. The electric polarization changes sign at each domain wall and varies six times along a loop encircling the vortex line. These vortices and anti-vortices are the cloverleaf defects observed in ref. 24.

Figure 3c shows a vortex–anti-vortex pair configuration obtained by minimizing the energy for a given distance between these defects. The domain walls diverge radially from the vortex/anti-vortex core with the 60°-angle between neighbouring domain walls. Far from the core they bend and become parallel to minimize the total length of the structural boundaries, which gives rise

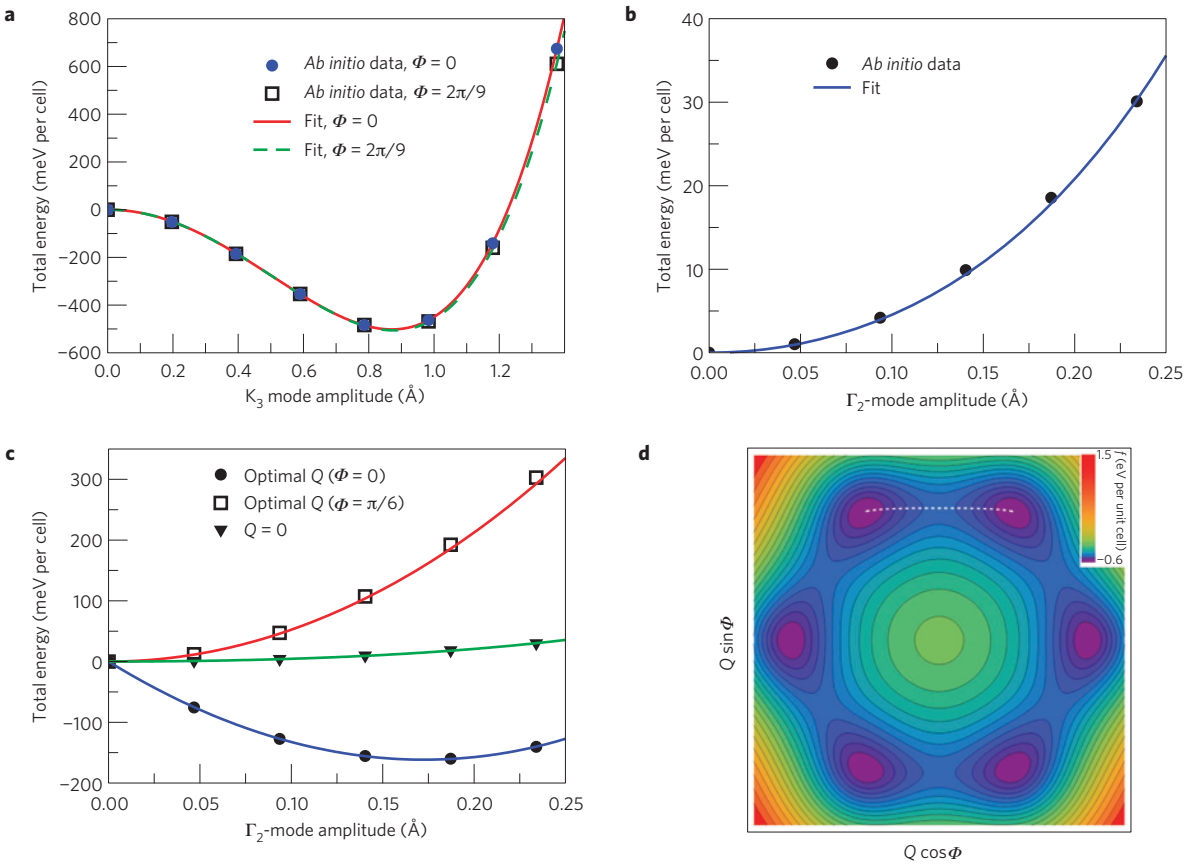

Figure 2 | Extraction of model parameters from *ab initio* calculations. a, Variation of total energy with respect to K_3 mode amplitude for two trimerization angles, $\Phi = 0$ and $\Phi = 2\pi/9$. Parameters a, b, c and c' are extracted, and owing to the weak angular dependence of the energy c' is small. **b**, Variation of total energy about the high-symmetry $P6_3/mmc$ structure with respect to the amplitude of the Γ_2^- (polar) mode, $\mathcal{P}$. The polar mode is stable and does not spontaneously emerge at $T = 0$ K. **c**, Coupling between K_3 and Γ_{2-} modes for two different trimerization angles. For trimerization angles of $0, \pm\pi/3, \pm 2\pi/3$ and π the anharmonic coupling leads to a non-zero polarization and a total energy lowering of ~ 26 meV per formula unit. On the other hand, intermediate trimerization angles do not allow polarization to develop. The g and g' parameters are extracted from these data. **d**, Contour plot of the free energy of uniformly trimerized states as a function of Q and Φ. Here, P_z has been optimized for each Q, Φ. The trajectory $Q(\Phi)$ (white dashed line) connecting two neighbouring energy minima corresponds to the lowest-energy structural domain wall.

to a linear potential between the discrete vortices as opposed to the logarithmically growing potential for continuous vortices.[30] Despite this confining potential, vortex lines and domain walls form dense networks[24–27] that are snapshots of states close to critical temperature capturing the formation of these topological defects by large thermal fluctuations[31,32].

A different type of topologically stable domain pattern is uncovered by considering the lowest-order coupling of the inhomogeneous trimerization to strains, which has the form

$$f_{\text{strain}} = -GQ^2[(u_{xx} - u_{yy})\partial_x \Phi - 2u_{xy}\partial_y \Phi]$$

where (x, y) are the Cartesian coordinates in the ab plane. With such a coupling, a parallel array of structural domain walls, each with the same increment of the trimerization angle ($\Delta\Phi = \pm\pi/3$), is topologically stable (Fig. 3d). Owing to the alternating electric polarization at the structural walls, such a Φ-staircase is at the same time a ferroelectric stripe domain state, similar to those stabilized in thin films by the long-range dipole–dipole interactions[33,34].

Magnetic defects

Next we address the coupling between the magnetism and the structural/ferroelectric domain walls. The spins of the Mn ions in hexagonal manganites order in one of four different magnetic states: A_1, A_2, B_1, and B_2, shown in Fig. 1d–g[35]. Their origin can be understood by considering the hierarchy of spin interactions. By far the strongest is the antiferromagnetic exchange between neighbouring spins in the triangular layers of Mn ions, which leads to the non-collinear 120° spin ordering. The magnetic easy-plane anisotropy, and the anti-symmetric Dzyaloshinskii–Moriya interaction with the Dzyaloshinskii vector along the c axis, confine spins to the ab plane. The local in-plane anisotropy axes, also favouring the 120° spin angle on neighbouring Mn sites, selects either the radial (as in the A_2 and B_1 phases) or the tangential (as in A_1 and B_2 phases) orientation of spins (Fig. 1). Finally, the interlayer exchange interactions, which are more than two orders of magnitude weaker than the intra-layer interactions, lead to either even (A phases) or odd (B phases) symmetry under the two-fold screw rotation $\tilde{2}_c$ (ref. 36).

Owing to the strong in-plane exchange, the angle between neighbouring spins remains close to 120° throughout a magnetic domain wall. Furthermore, to match the directions of spins on both sides of the wall with the local in-plane anisotropy axes, the spins in the domain wall must rotate in the ab plane. Therefore, the structure of magnetic domain walls can be described by two angles, (ψ_1, ψ_2), quantifying the rotation of spins around the c axis in the even and odd layers respectively[21,35] as shown in Fig. 1h. The transformation properties

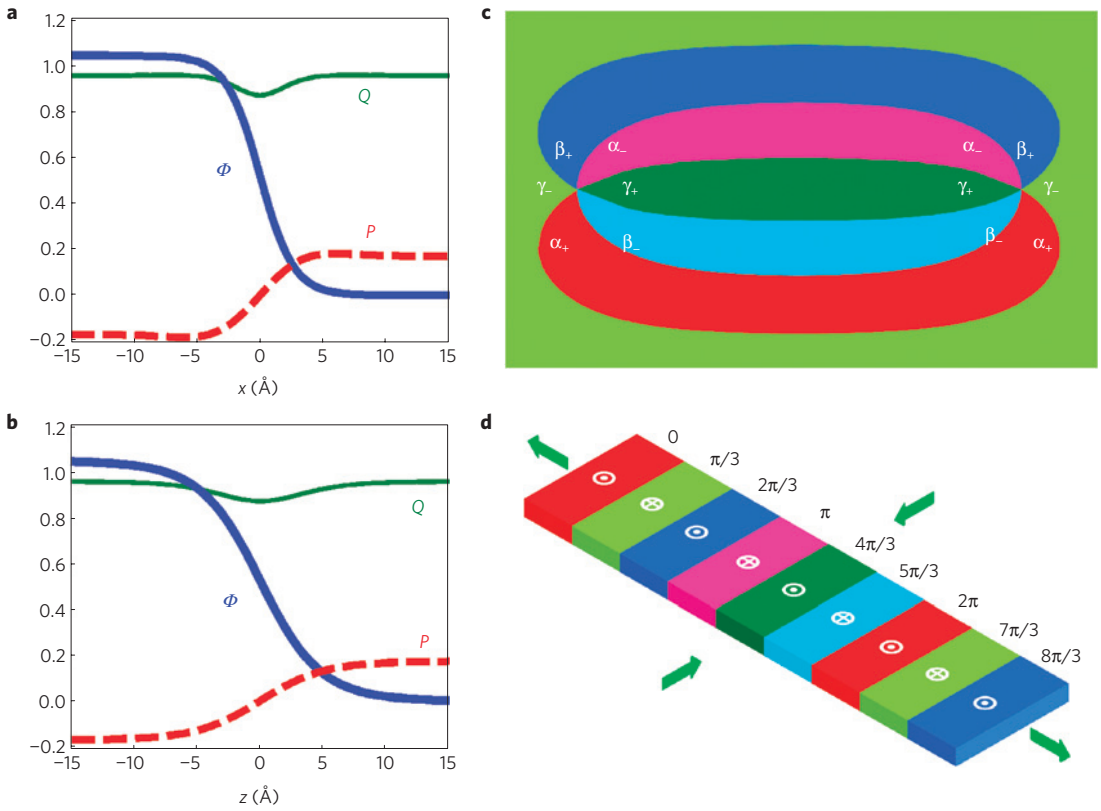

Figure 3 | Structural topological defects. a,**b**, The variation of the trimerization angle Φ (measured in radians, thick blue line), trimerization amplitude Q (measured in Å, thin green line) and the polar mode $\mathcal{P}$ (measured in Å, dashed red line) across the lowest-energy domain wall normal to the *ab* plane (**a**) and parallel to the *ab* plane (**b**). **c**, The vortex–antivortex pair. In the structural vortex/antivortex the angle Φ increases/decreases by 2π along the loop encircling the vortex core in the anticlockwise direction (the six trimerization states are indicated by colour). **d**, The topological stripe domain state with the alternating polarization (white symbols) along the *c* axis. A strain indicated by green arrows results in the monotonic increase of Φ in the direction normal to the stripes.

of ψ_1 and ψ_2 (Table 1) determine the form of the magnetic free-energy density:

$$\begin{aligned} f_{\mathrm{mag}}(\psi_1,\psi_2,H_c) &= S[(\partial_\mu\psi_1)^2+(\partial_\mu\psi_2)^2] \\ &+ A[\sin^2\chi_1+\sin^2\chi_2]-C_+\cos(\chi_1+\chi_2) \\ &- C_-\cos(\chi_1-\chi_2)-\frac{1}{2}M_{\mathrm{A}_2}H_c(\sin\chi_1+\sin\chi_2) \end{aligned} \qquad (2)$$

where $\chi_{1,2}=\psi_{1,2}-\Phi$. The first term originates from the nearest-neighbour exchange. Comparing the energies of the four uniform phases (Fig. 1): $f_{\mathrm{B}_2}=-C_+-C_-$, $f_{\mathrm{A}_1}=C_++C_-$, $f_{\mathrm{A}_2}=2A-C_++C_-$ and $f_{\mathrm{B}_1}=2A+C_+-C_-$, we conclude that the A coefficient results from the in-plane magnetic anisotropy, C_+ describes the interlayer exchange interactions, and C_- is related to an interlayer symmetric exchange anisotropy. The last term in equation (2) describes the weak ferromagnetic moment along the *c* axis in the A_2 phase with $(\chi_1,\chi_2)=\pm(\pi/2,\pi/2)$. Terms proportional to spin operators of power higher than 2 are neglected. The values of the parameters of the magnetic free energy (equation (2)), used to calculate the magnetic structure of the topological defects, can be found in Supplementary Table I.

We first consider magnetic domain walls within one structural domain $\Phi=0$, in which case $\chi_{1,2}=\psi_{1,2}$. The walls separate two magnetic states related by the time-reversal operation, so that $\Delta\psi_{1,2}=\pm\pi$ across the wall. Figure 4a,b shows two topologically distinct types of such walls between the degenerate B_2 states: the one in which spins in neighbouring layers rotate in opposite ($\Delta\psi_1=\Delta\psi_2=\pi$) and the same ($\Delta\psi_1=-\Delta\psi_2=\pi$) directions. The free energies per unit area of the two walls are $8\sqrt{S(A+C_+)}$ and $8\sqrt{S(A+C_-)}$ respectively. The domain wall with $\psi_1=\psi_2$ has a non-zero magnetic moment, because the magnetic configuration in the middle of the wall, $(\psi_1(0),\psi_2(0))=(\pi/2,\pi/2)$, is of the weakly ferromagnetic A_2 type. The net magnetic moment per unit area of the wall is $M_{\mathrm{A}_2}l_+$, where M_{A_2} is the magnetization in the A_2 phase and $l_\pm=\pi\sqrt{S/(A+C_\pm)}$ is the domain-wall thickness.

Importantly, within a domain, the reference triangles of Mn spins that are used to define the four magnetic phases have their apical oxygen ions tilted either towards or away from a common centre (Fig. 1). The tilts of the oxygen bipyramids, described by the angle Φ, determine the in-plane magnetic anisotropy axes. A shift by one lattice constant (of the non-trimerized lattice) within the uniform domain results in a 120° rotation of the anisotropy axes, because $\Phi\rightarrow\Phi+2\pi/3$. To minimize the magnetic energy, therefore, ψ_1 and ψ_2 must transform in the same way: $\psi_{1,2}\rightarrow\psi_{1,2}+2\pi/3$. This is why the free energy equation (2) depends on $\chi_{1,2}=\psi_{1,2}-\Phi$, and why, in general, the covariant angles (χ_1,χ_2), rather than (ψ_1,ψ_2), should be used to describe the magnetic phases.

Now considering structural inhomogeneity, it is evident that the magnetic ordering must respond to the presence of a structural domain wall. At a structural domain wall with $\Delta\Phi=\pi/3$, for example, spins rotate either by $\pi/3$, in which case χ is the same on both sides of the wall, or by $-2\pi/3$, in which case $\Delta\chi=-\pi$. Thus, structural domain walls are also magnetic domain walls. In the lowest-energy configuration, $\Delta\psi_1=\Delta\psi_2=\pi/3$ (Fig. 4c), whereas the next-lowest-energy configuration has $\Delta\psi_1=\Delta\psi_2=-2\pi/3$ (Fig. 4d). Domain walls in which spins in neighbouring layers rotate over different angles, for example $\Delta\psi_1=\pi/3$ and $\Delta\psi_2=-5\pi/3$,

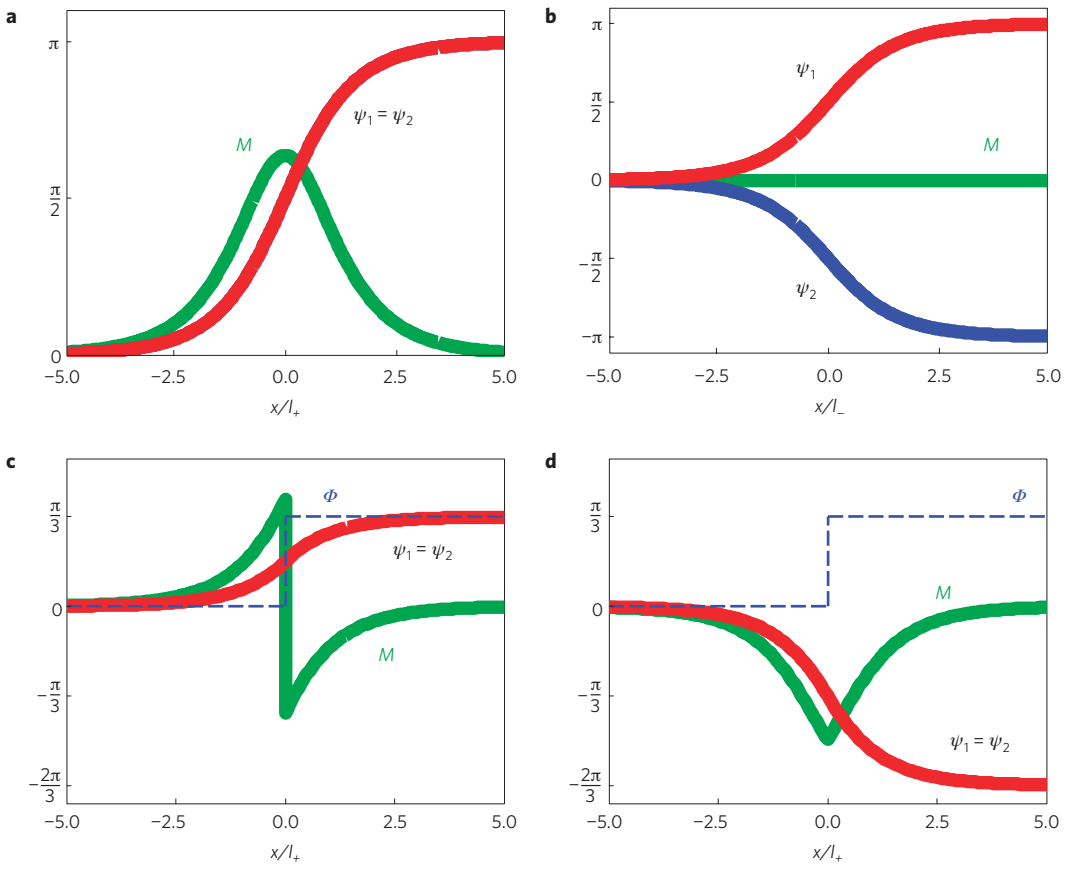

Figure 4 | Antiferromagnetic domain walls in hexagonal manganites. a,**b**, Free; 180° walls within one structural domain. **c**,**d**, Domain walls clamped to structural boundaries. Shown is the variation of the spin rotation angles ψ_1 and ψ_2 (solid red and blue lines, respectively), magnetization M_c (solid green line, arbitrary units) and the trimerization phase Φ (dashed blue line) across the domain wall. At the structural boundary Φ and the directions of magnetic easy axes on Mn sites change by 60°. The directions of spins adjust over much longer distances by rotating over the 60° (**c**) or −120° (**d**) angle.

are higher in energy. It is important to stress that the thickness of the magnetic domain walls—$l_+ \sim 40$ Å and $l_- \sim 90$ Å—greatly exceeds that of the structural domain wall. The $\Delta\psi = -2\pi/3$ antiferromagnetic domain wall clamped to the structural boundary (Fig. 4d) has a non-zero moment along the c axis equal to $-2/3M_{A_2}l_+$ per unit area of the wall.

With these considerations, we can understand the simultaneous presence of clamped and free antiferromagnetic domain walls in hexagonal manganites[14]. Every structural domain wall ($\Delta\Phi = \pi/3$) induces a magnetic domain wall in which spins rotate by 60° or 120° (Fig. 4c,d). Owing to the sign change of electric polarization at the structural boundary, these antiferromagnetic domain walls seem to be clamped with the ferroelectric domain walls. The free antiferromagnetic domain walls that do not follow ferroelectric domain boundaries are the 180° antiferromagnetic domain walls within one structural domain (Fig. 4a,b). These results imply that in the minimal-energy magnetic state of the structural vortex spins wind around the vortex core, and the total spin rotation angle along a loop encircling the vortex is $\Delta\psi_1 = \Delta\psi_2 = \Delta\Phi = \pm 2\pi$. That is, structural vortices are also magnetic vortices. The small-angle neutron scattering experiment on $HoMnO_3$, the electric switching of magnetization of coupled ferromagnetic/$LuMnO_3$ thin films and the magnetic force microscopy study of $ErMnO_3$ all indicated the presence of an uncompensated ferromagnetic moment at antiferromagnetic domain walls[12,37,38]. Our analysis summarized in Fig. 4 shows that both clamped and free antiferromagnetic domain walls induce magnetization along the c axis in their vicinity and several of them have a net magnetic moment. Although the weak ferromagnetic moment—arising from canting of Mn spins—is small, it can be significantly enhanced by the magnetization of rare-earth ions coupled to Mn spins, as in the bulk A_2 phase[39].

Conclusions

Hexagonal manganites show a rich variety of topological defects resulting from the coexistence of three broken-symmetry states: a periodic lattice distortion, ferroelectricity and a non-collinear magnetism. Despite the vastly different energy and length scales, these three orders are entangled at the defects. Our phenomenological theory with coefficients extracted from first-principles calculations explains many unusual physical properties of topological defects in hexagonal manganites, for example the origin of discrete vortices, the clamped structural, ferroelectric and magnetic domain walls coexisting with free magnetic domain walls as well as the ferromagnetism at antiferromagnetic walls. A surprising outcome of this work is that the sharpness of the structural domain walls in hexagonal manganites results from the strong nonlinear coupling between the lattice trimerization and electric polarization. We calculated the spin structure of domain walls and predicted a new topological stripe state under an applied strain. Our study shows that the coupling between ferroelectricity and magnetism in topological defects can be strong even when the bulk magnetoelectric coupling is forbidden by symmetry, which opens a route to high-temperature multiferroics with electrically switchable magnetization.

Methods

We performed *ab initio* calculations using Kohn–Sham density functional theory (DFT), as implemented in the ABINIT software package[40,41]. All calculations employ a supercell approach with periodic boundary conditions. Wavefunctions

and charge densities are expanded in a plane-wave basis. Efficient computational treatment of heavy elements is achieved using the projector-augmented wave method for core–valence partitioning[42], which significantly reduces the required plane-wave energy cutoff.

We approximate the Kohn–Sham exchange-correlation potential using the local spin density approximation[43] with a Hubbard-U correction applied to the partially filled manganese d states following the Liechtenstein approach[44,45] with double-counting corrections in the fully localized limit. All calculations reported here were performed with values of $U = 8.0$ eV for the Coulomb integrals and $J = 0.88$ eV for the intra-atomic exchange coupling, as chosen previously in ref. 17. We enforce an A-type antiferromagnetic ordering for all calculations[17]. With this choice of parameters and magnetic ordering, an insulating electronic structure in the high-symmetry ($P6_3/mmc$) crystal structure results, with a Kohn–Sham bandgap of 0.75 eV. As this underestimates experimentally reported values of the bandgap[46], we carefully verified that no spurious metal–insulator transitions occur as structural distortions are introduced, so that the free-energy landscape contains no anomalous features.

The parameters given in equation (1) can be extracted by considering homogeneously distorted periodic structures that are commensurate with the wavevectors of all distortions. The smallest unit cell that can accommodate all possible values of Q, Φ and $\mathcal{P}$ contains 30 atoms, or 6 formula units of $YMnO_3$. We do not impose directly a constraint on the value of P_c. Rather, we impose the magnitude of the Γ_2^- mode on the structure, which results in $P_c \neq 0$. To fit the parameters, we explore the variation of the DFT total energy with the magnitude of Q, Φ and $\mathcal{P}$. The ionic positions are defined by the projection of the DFT ground-state P6 $_3$ cm structure onto the Γ_2^- and K_3 modes of $P6_3/mmc$ combined with the desired value of Q, Φ and $\mathcal{P}$. However, we fully optimize the cell parameters for each mode distortion to eliminate stresses. The result is that the homogeneous contribution to stresses has been implicitly eliminated through renormalization of the Landau parameters.

The dependence of the free energy on $\mathcal{P}$ with $Q = 0$ is shown in Fig. 2b, reaffirming the stability of the polar mode in the high-symmetry structure, and therefore the improper nature of the ferroelectricity in $YMnO_3$. Figure 2a and Fig. 2c respectively show computations for the trimerization mode and the coupling between trimerization and polar modes.

With all homogeneous Landau parameters given in equation (1) specified, we now turn our attention to the stiffness parameters. The most convenient way to proceed is to write the spatial inhomogeneity in Q and $\mathcal{P}$ as a single harmonic, for example $Q(\mathbf{r}) = Q_q e^{i\mathbf{q}.\mathbf{r}}$ with $\Phi = 0$. The stiffness energy has then the form

$$f_s(\mathbf{q}) = \frac{1}{2}\sum_i q_i^2 [s_Q^i |Q_q|^2 + s_P^i |\mathcal{P}_q|^2]$$

This expression is harmonic in mode amplitudes Q_q and $\mathcal{P}_q$. Note that to compute s_Q^i, we do not need to consider spatial variations in the Φ field. The computational cost of explicitly computing f_s by imposing various short wave vectors, q, in our supercell density-functional calculations would be prohibitive. Instead we extract these harmonic terms using the method of frozen phonons combined with Fourier interpolation of the inter-atomic force constants, a method commonly used for computing phonon band structures. We note that this approach is consistent with the choice of using symmetry-adapted modes for parameterizing the local terms, because the relevant symmetry-adapted distortions consist of individual normal lattice modes. Supplementary Fig. 1 shows our calculated phonon band structure for the high-symmetry structure ($P6_3/mmc$) of $YMnO_3$. The strongest instability at the K point is the cell-tripling K_3 trimerization mode. As previously noted, all Γ phonons, including the Γ_2^- polar mode, are stable in the high-symmetry structure.

Multiplying the dynamical matrix used in the computation of phonon modes by the weighted mass, we obtain a $\mathbf{q}$-dependent force-constant matrix:

$$C_{i,j}(\mathbf{q}) = \sqrt{M_i M_j} D_{i,j}(\mathbf{q})$$

and by identifying the relevant branch, the $\mathbf{q}$-dependent eigenvalues of $C_{i,j}(\mathbf{q})$ are related to $\partial^2 f_s/\partial Q_0^2$ or $\partial^2 f_s/\partial \mathcal{P}_0^2$. Hence, the required stiffness parameters can be extracted. As an example, Supplementary Fig. 1 shows the extraction of s_Q^x by fitting the q_x dispersion of the force constant of the unstable trimerization branch. Using this technique, we find the stiffness parameters for $YMnO_3$ listed in Table 2.

Received 18 April 2012; accepted 20 September 2013; published online 27 October 2013

References

1. Cheong, S-W. & Mostovoy, M. Multiferroics: A magnetic twist for ferroelectricity. *Nature Mater.* **6,** 13–20 (2007).
2. Ramesh, R. & Spaldin, N. A. Multiferroics: Progress and prospects in thin films. *Nature Mater.* **6,** 21–29 (2007).
3. Khomskii, D. Trend: Classifying multiferroics: Mechanisms and effects. *Physics* **2,** 20 (2009).
4. Kimura, T. *et al.* Magnetic control of ferroelectric polarization. *Nature* **426,** 55–58 (2003).
5. Hur, N. *et al.* Electric polarization reversal and memory in a multiferroic material induced by magnetic fields. *Nature* **429,** 392–395 (2004).
6. Kitagawa, Y. *et al.* Low-field magnetoelectric effect at room temperature. *Nature Mater.* **9,** 797–802 (2010).
7. Van Aken, B. B., Palstra, T. T. M., Filippetti, A. & Spaldin, N. A. The origin of ferroelectricity in magnetoelectric $YMnO_3$. *Nature Mater.* **3,** 164–170 (2004).
8. Neaton, J. B., Ederer, C., Waghmare, U. V., Spaldin, N. A. & Rabe, K. M. First-principles study of spontaneous polarization in multiferroic $BiFeO_3$. *Phys. Rev. B* **71,** 014113 (2005).
9. Lebeugle, D. *et al.* Electric-field-induced spin flop in $BiFeO_3$ single crystals at room temperature. *Phys. Rev. Lett.* **100,** 227602 (2008).
10. Chu, Y-H. *et al.* Electric-field control of local ferromagnetism using a magnetoelectric multiferroic. *Nature Mater.* **7,** 478–482 (2008).
11. Lebeugle, D., Mougin, A., Viret, M., Colson, D. & Ranno, L. Electric field switching of the magnetic anisotropy of a ferromagnetic layer exchange coupled to the multiferroic compound $BiFeO_3$. *Phys. Rev. Lett.* **103,** 257601 (2009).
12. Skumryev, V. *et al.* Magnetization reversal by electric-field decoupling of magnetic and ferroelectric domain walls in multiferroic-based heterostructures. *Phys. Rev. Lett.* **106,** 057206 (2011).
13. Fennie, C. J. Ferroelectrically induced weak ferromagnetism by design. *Phys. Rev. Lett.* **100,** 167203 (2008).
14. Fiebig, M., Lottermoser, Th., Fröhlich, D., Goltsev, A. V. & Pisarev, R. V. Observation of coupled magnetic and electric domains. *Nature* **419,** 818–820 (2002).
15. Yakel, H. L., Koehler, W. C., Bertaut, E. F. & Forrat, E. F. On the crystal structure of the manganese(III) trioxides of the heavy lanthanides and yttrium. *Acta Crystallogr.* **16,** 957–962 (1963).
16. Katsufuji, T. *et al.* Dielectric and magnetic anomalies and spin frustration in hexagonal $RMnO_3$ (R = Y, Yb, and Lu). *Phys. Rev. B* **64,** 104419 (2001).
17. Fennie, C. J. & Rabe, K. M. Ferroelectric transition in $YMnO_3$ from first principles. *Phys. Rev. B* **72,** 100103 (2005).
18. Dela Cruz, C. *et al.* Strong spin-lattice coupling in multiferroic $HoMnO_3$: Thermal expansion anomalies and pressure effect. *Phys. Rev. B* **71,** 060407 (2005).
19. Lee, S. *et al.* Giant magneto-elastic coupling in multiferroic hexagonal manganites. *Nature* **451,** 805–808 (2008).
20. Adem, U. *et al.* Scaling behavior of the magnetocapacitance of $YbMnO_3$. *J. Phys.: Condens. Matter* **21,** 496002 (2009).
21. Goltsev, A. V., Pisarev, R. V., Lottermoser, T. & Fiebig, M. Structure and interaction of antiferromagnetic domain walls in hexagonal $YMnO_3$. *Phys. Rev. Lett.* **90,** 177204 (2003).
22. Hanamura, E., Hagita, K. & Tanabe, Y. Clamping of ferroelectric and antiferromagnetic order parameters of $YMnO_3$. *J. Phys. Condens. Matter* **15,** L103–L109 (2003).
23. Hanamura, E. & Tanabe, Y. Ferroelectric and antiferromagnetic domain wall. *J. Phys. Soc. Jpn.* **72,** 2959–2966 (2003).
24. Choi, T. *et al.* Insulating interlocked ferroelectric and structural antiphase domain walls in multiferroic $YMnO_3$. *Nature Mater.* **9,** 253–258 (2010).
25. Chae, S. C. *et al.* Self-organization, condensation, and annihilation of topological vortices and antivortices in a multiferroic. *Proc. Natl Acad. Sci. USA* **107,** 21366–21370 (2010).
26. Jungk, T., Hoffmann, Á., Fiebig, M. & Soergel, E. Electrostatic topology of ferroelectric domains in $YMnO_3$. *Appl. Phys. Lett.* **97,** 012904 (2010).
27. Lilienblum, M., Soergel, E. & Fiebig, M. J. Manipulation of ferroelectric vortex domains in hexagonal manganites. *J. Appl. Phys.* **110,** 052007 (2011).
28. Mostovoy, M. Multiferroics: A whirlwind of opportunities. *Nature Mater.* **9,** 188–190 (2010).
29. Kumagai, Y. & Spaldin, N. Structural domain walls in polar hexagonal manganites. *Nature Commun.* **4,** 1540 (2013).
30. Chaikin, P. M. & Lubensky, T. C. *Principles of Condensed Matter Physics* (Cambridge Univ. Press, 1995).
31. Kaski, K., Grant, M. & Gunton, J. D. Domain growth in the clock model. *Phys. Rev. B* **31,** 3040–3047 (1985).
32. Grest, G. S., Anderson, M. P. & Srolovitz, D. J. Domain-growth kinetics for the Q-state Potts model in two and three dimensions. *Phys. Rev. B* **38,** 4752–4760 (1988).
33. Fong, D. D. *et al.* Ferroelectricity in ultrathin perovskite films. *Science* **304,** 1650–1653 (2004).
34. Matsumoto, T. & Okamoto, M. J. Effects of electron irradiation on the ferroelectric 180° in-plane nanostripe domain structure in a thin film prepared from a bulk single crystal of $BaTiO_3$ by focused ion beam. *J. Appl. Phys.* **109,** 014104 (2011).
35. Fiebig, M., Lottermoser, T. & Pisarev, R. V. Spin-rotation phenomena and magnetic phase diagrams of hexagonal $RMnO_3$. *J. Appl. Phys.* **93,** 8194–8196 (2003).
36. Sato, T. J. *et al.* Unconventional spin fluctuations in the hexagonal antiferromagnet $YMnO_3$. *Phys. Rev. B* **68,** 014432 (2003).

37. Ueland, B., Lynn, J. W., Laver, M., Choi, Y. J. & Cheong, S-W. Origin of electric-field-induced magnetization in multiferroic $HoMnO_3$. *Phys. Rev. Lett.* **104,** 147204 (2010).
38. Geng, Y., Lee, N., Choi, Y. J., Cheong, S-W. & Wu, W. Collective magnetism at multiferroic vortex domain walls. *Nano Lett.* **12,** 6055–6059 (2012).
39. Sugie, H., Iwata, N. & Kohn, K. J. Magnetic ordering of rare earth ions and magnetic-electric interaction of hexagonal $RMnO_3$ (R = Ho, Er, Yb or Lu). *J. Phys. Soc. Jpn.* **71,** 1558–1564 (2002).
40. Gonze, X. *et al.* First-principles computation of material properties: The ABINIT software project. *Comput. Mater. Sci.* **25,** 478–492 (2002).
41. Gonze, X. *et al.* A brief introduction to the ABINIT software package. *Z. Kristallogr.* **220,** 558–562 (2005).
42. Torrent, M., Jollet, F., Bottin, F., Zerah, G. & Gonze, X. Implementation of the projector augmented-wave method in the ABINIT code: Application to the study of iron under pressure. *Comput. Mater. Science* **42,** 337–351 (2008).
43. Perdew, J. P. & Wang, Y. Accurate and simple analytic representation of the electron-gas correlation energy. *Phys. Rev. B* **45,** 13244–13249 (1992).
44. Amadon, B., Jollet, F. & Torrent, M. γ and β cerium: LDA+U calculations of ground-state parameters. *Phys. Rev. B* **77,** 155104 (2008).
45. Liechtenstein, A. I., Anisimov, V. I. & Zaanen, J. Density-functional theory and strong interactions: Orbital ordering in Mott-Hubbard insulators. *Phys. Rev. B* **52,** R5467–R5470 (1995).
46. Smith, A. E. *et al.* Mn^{3+} in trigonal bipyramidal coordination: A new blue chromophore. *J. Am. Chem. Soc.* **131,** 17084–17086 (2009).
47. King-Smith, R. D. & Vanderbilt, D. Theory of polarization of crystalline solids. *Phys. Rev. B* **47,** 1651–1654 (1993).

Acknowledgements

We are grateful to S-W. Cheong for discussions of the stripe state. S.A. and M.M. were supported by the ZIAM Groningen under award MSC06-20 and by FOM grant 11PR2928. K.T.D. acknowledges fellowship support from the International Center of Materials Research. We acknowledge support from the Center for Scientific Computing from the CNSI, MRL, an NSF MRSEC grant (DMR-1121053) and Hewlett Packard. N.A.S. was supported by the ETH Zürich.

Additional information

Supplementary information is available in the online version of the paper. Reprints and permissions information is available online at www.nature.com/reprints. Correspondence and requests for materials should be addressed to M.M.

Competing financial interests

The authors declare no competing financial interests.